CARDIFF UNIVERSITY
PRIFYSGOL CAERDYDD

ORCA – Online Research @ Cardiff

This is an Open Access document downloaded from ORCA, Cardiff University's institutional repository:https://orca.cardiff.ac.uk/id/eprint/176497/

This is the author's version of a work that was submitted to / accepted for publication.

Citation for final published version:

Peng, Mi, Ge, Yuzhen, Gao, Rui, Yang, Jie, Li, Aowen, Xie, Zhiheng, Yu, Qiaolin, Zhang, Jie, Asakura, Hiroyuki, Zhang, Hui, Liu, Zhi, Zhang, Qi, Deng, Jin, Zhou, Jihan, Zhou, Wu, Hutchings, Graham J and Ma, Ding 2025. Thermal catalytic reforming for hydrogen production with zero CO2 emission. Science 387 (6735) , pp. 769-775. 10.1126/science.adt0682

Publishers page: https://doi.org/10.1126/science.adt0682

Please note:
Changes made as a result of publishing processes such as copy-editing, formatting and page numbers may not be reflected in this version. For the definitive version of this publication, please refer to the published source. You are advised to consult the publisher's version if you wish to cite this paper.

This version is being made available in accordance with publisher policies. See http://orca.cf.ac.uk/policies.html for usage policies. Copyright and moral rights for publications made available in ORCA are retained by the copyright holders.

Thermal catalytic reforming for hydrogen production with zero CO_2 emission

Mi Peng[1]†, Yuzhen Ge[1]†, Rui Gao[2]†, Jie Yang[3]†, Aowen Li[4]†, Zhiheng Xie[1], Qiaolin Yu[1], Jie Zhang[1], Asakura Hiroyuki[5], Hui Zhang[6], Zhi Liu[7], Qi Zhang[8], Jin Deng[3], Jihan Zhou[1]*, Wu Zhou[4]*, Graham J. Hutchings[9*], Ding Ma[1]*

Affiliations:

[1] Beijing National Laboratory for Molecular Science, New Cornerstone Science Laboratory, College of Chemistry and Molecular Engineering, Peking University; Beijing, China.

[2] School of Chemistry and Chemical Engineering, Inner Mongolia University; Hohhot, China.

[3] CAS Key Laboratory of Urban Pollutant Conversion, Anhui Province Key Laboratory of Biomass Clean Energy, Department of Applied Chemistry, University of Science and Technology of China; Hefei, China.

[4] School of Physical Sciences, University of Chinese Academy of Sciences; Beijing, China.

[5] Department of Applied Chemistry, Faculty of Science and Engineering, Kindai University; Osaka, Japan.

[6] Shanghai Synchrotron Radiation Facility, Shanghai Advanced Research Institute, Chinese Academy of Sciences; Shanghai, China.

[7] Center for Transformative Science, Shanghai Tech University; Shanghai, China.

[8] SINOPEC Shanghai Research Institute of Petrochemical Technology Co., Ltd.; Shanghai, China.

[9] Max Planck-Cardiff Centre on the Fundamentals of Heterogeneous Catalysis, FUNCAT, Cardiff Catalysis Institute, School of Chemistry, Cardiff University; Cardiff, UK.

*Corresponding author. Email: dma@pku.edu.cn, wuzhou@ucas.ac.cn, jhzhou@pku.edu.cn, Hutch@Cardiff.ac.uk

†These authors contributed equally to this work.

Abstract: Carbon neutral hydrogen production is of key importance for the chemical industry of the future. Here, we demonstrate a new thermal catalytic route for the partial reforming of ethanol into hydrogen and acetic acid with near-zero CO_2 emissions. This reaction is enabled by a catalyst containing a high density of atomic Pt_1 and Ir_1 species supported on a reactive α-MoC substrate, achieving a hydrogen production rate of 331.3 millimoles of hydrogen per gram catalyst per hour and an acetic acid selectivity of 84.5% at 270 °C, and is therefore more energy-efficient compared with standard reforming. Techno-economic analysis of partial ethanol reforming demonstrates the potential profitability for operation at an industrial scale, presenting the opportunity to produce hydrogen and acetic acid with a significantly reduced carbon dioxide footprint.

Main Text:

The reforming of fossil fuels is currently the predominant route for industrial hydrogen (H_2) production (*1, 2*), but is associated with substantial CO_2 emissions (*3*). Greener alternatives, such as water electrolysis (*4*) and biomass gasification (*5*), could reduce the carbon footprint of H_2 production, but face bottlenecks in efficiency, cost-effectiveness and scalability. Partial oxidation ($C_2H_5OH + 1.5O_2 = 2CO_2 + 3H_2$) and full steam reforming ($C_2H_5OH + 3H_2O = 2CO_2 + 6H_2$) (*6, 7*) of ethanol have also been actively explored for possible carbon-neutral H_2 production, especially using bio-derived renewable ethanol. Although these processes show some advantages over conventional H_2 production routes (Fig. 1A) (*8*), partial oxidation is intrinsically limited by the stoichiometrically low H_2 production rate (*9*), whereas the highly endothermic nature of full steam reforming (Fig. 1B) (*10, 11*) requires high operating temperatures that promote undesired side reactions (*12*). Notably, both pathways convert 100% of the carbon atoms into CO_2, depleting the carbon resources.

Reaction pathway and catalyst design

A comprehensive exploration of the ethanol reforming process revealed a complex reaction network (Fig. 1C). An ideal H_2 production pathway from ethanol reforming should both be thermodynamically favorable and minimize net carbon emission (*13*). We propose selective partial reforming of ethanol with water to form acetic acid and H_2 ($C_2H_5OH + H_2O = CH_3COOH + 2H_2$) as the more valuable route (rust red in Fig. 1C). It offers multiple benefits: (i) the reforming process extracts H_2 from both ethanol and water, producing more H_2 than the dehydrogenation process from a stoichiometric perspective; (ii) carbon atoms remain in the liquid phase, generating a valuable chemical product and minimizing CO_2 emission; (iii) the co-produced acetic acid fulfills rising global demand and serves as a critical intermediate for the production of additional chemicals, including cellulose acetate, vinyl acetate monomer, polyvinyl acetate (*14*). In contrast, conventional catalysts for ethanol reforming, including noble metal catalysts (such as Pt and Pd) and non-noble metal catalysts (such as, Ni, Cu, and Co) (*15-21*), tend to convert the carbon atoms in ethanol into CO_x, leading to a net carbon-positive process with CO_x emission (without taking into account the origin of ethanol).

Designing a new catalyst that enables the reforming reaction while preventing C-C bond breakage (*22*) is crucial for selectively facilitating this partial reforming route into acetic acid. We developed a highly dispersed Pt/Ir metal catalyst supported on α-MoC that efficiently promoted the partial steam reforming of ethanol into H_2 and acetic acid under temperatures considerably lower than that required in conventional ethanol steam reforming. We selected α-MoC as a reactive support to construct the interfacial catalysts in view of its unprecedented capability of activating water at low temperatures (*23, 24*) and its strong interactions with noble metals, which created a high density of interfacial active sites for methanol reforming (*25, 26*).

Compared to methanol reforming, ethanol reforming is thermodynamically less favored (*27, 28*) and requires a higher density of reforming sites to facilitate the reaction. More importantly, to achieve a high selectivity towards acetic acid, the cleavage of the C-C bond in the ethanol backbone, which leads to the formation of undesired C_1 products like CO, CO_2 or CH_4 (see Figure 1C), must be suppressed. Because C-C bond cleavage typically requires a di-σ carbon-metal

configuration, large metal catalytic ensembles that contain abundant metal-metal bonds must be eliminated (*29*). Previous studies on Ir/α-MoC and Pt/α-MoC catalysts revealed that Ir has a stronger interaction with α-MoC (*26, 30, 31*), which leads to much higher dispersion than Pt under the same metal loading, although the intrinsic dehydrogenation activity of Ir is lower than that of Pt (*26, 32*). We expected co-loading of Ir and Pt onto α-MoC improve Pt dispersion, thereby constructing a catalyst (M/α-MoC, M = Pt/Ir) with a high density of atomic interfacial sites (i.e. active interfaces formed by atomic-scale Pt or Ir species, including Pt or Ir single atoms as well as fully exposed clusters (*33*), over the reactive α-MoC support) that are beneficial for the efficient and selective reforming of ethanol into acetic acid.

Catalyst synthesis and characterization

We synthesized a series of Pt/Ir-based catalysts supported on α-MoC using the incipient wetness impregnation method (see Methods for details; the number before Pt or Ir denotes the weight percentage of the metal loading). X-ray diffraction (XRD) revealed the formation of Pt particles ($2\theta = 39.8^{o}$) in 3Pt/α-MoC, and the diffraction for crystalline Pt became more pronounced in 6Pt/α-MoC (Fig. 2A, Fig. S1). In contrast, Ir particles were not detected even at a metal loading of 6 wt% (Fig. 2A, Fig. S2). Importantly, with the addition of Ir, 3Pt3Ir/α-MoC did not show obvious XRD peaks for either Pt or Ir crystals at a total metal loading of 6 wt%, confirming that Ir indeed enhanced the dispersion of Pt species. Loading the Pt and Ir species with equal concentration onto an inert SiO_2 support (3Pt3Ir/SiO_2) produced metal particles that were resolved by XRD (Figure 2A). This 3Pt3Ir/SiO_2 catalyst served as a reference catalyst containing abundant large metal ensemble sites.

The metal dispersions were further analyzed using extended x-ray absorption fine-structure (EXAFS). For the 1Pt/α-MoC catalyst, the Pt-Pt coordination number (CN) was 1.0, indicating the formation of small Pt clusters even at a low Pt loading. The average $CN_{Pt\text{-}Pt}$ increased with higher Pt loading, reaching 4.9 for 6Pt/α-MoC (Fig. 2B, Fig. S3 to S8, Tables S2 and S3), suggesting the formation of a substantial number of Pt ensemble sites. In contrast, no Ir-Ir coordination was detected in the 1Ir/α-MoC and 3Ir/α-MoC catalysts, and the average $CN_{Ir\text{-}Ir}$ for 6Ir/α-MoC was only 1.9, indicating a much higher dispersion of Ir on α-MoC compared to Pt (Fig. 2B). At a total metal loading of 6 wt%, the 3Pt3Ir/α-MoC catalyst showed no Ir-Ir scattering and a $CN_{Pt\text{-}Pt}$ of 2.3, suggesting atomic dispersion of Ir species and enhanced dispersion of Pt compared to 3Pt/α-MoC.

We used atomic-number (Z) contrast imaging and electron energy-loss spectroscopy (EELS) mapping on aberration-corrected scanning transmission electron microscopy (STEM) to visualize the atomic-scale structures of the 3Pt/α-MoC and 3Pt3Ir/α-MoC catalysts. For 3Pt/α-MoC, STEM Z-contrast image combined with EELS mapping revealed the coexistence of atomically dispersed Pt species and Pt clusters with diameter about 1 nm (Fig. 2, C and D, Fig. S9 and S10). For 3Pt3Ir/α-MoC, the Z-contrast imaging could not differentiate Pt and Ir (Fig. S10), but the EELS mapping in Fig. 2F, in combination with the Z-contrast image in Fig. 2E, revealed the coexistence of atomically dispersed Pt and Ir species, as well as small Pt clusters on the α-MoC support. The Pt and Ir EELS signals extracted from Fig. 2F were highly confined to single pixels, demonstrating that the elemental-sensitive EELS mapping has single-atom sensitivity (*34*). In addition,

comparison of Fig. 2D to Fig. 2F revealed a much-improved dispersion of Pt species in 3Pt3Ir/α-MoC than that in 3Pt/α-MoC, consistent with the conclusion drawn from XAS.

Atomic electron tomography (AET) (*35, 36*) was used to investigate the three-dimensional (3D) distribution and coordination of Pt (and Ir) atoms in metal clusters in the 3Pt/α-MoC and 3Pt3Ir/α-MoC catalysts (see Methods and Figs. S11 to S13). Although sampling is limited with AET, it still provides valuable insights into the 3D distribution of the Pt(Ir) species on the α-MoC support, and the local metal-metal CNs calculated from the reconstructed atomic coordinates can be informative. In 3Pt/α-MoC, for a 1495-atom motif containing 48 Pt atoms, most Pt atoms had CN_{Pt-Pt} ranging from 3 to 9 (Fig. 2G, Movie S1). In contrast, in the 3Pt3Ir/α-MoC catalyst, most of the Pt/Ir atoms were present as single atoms distributed at point defect sites on α-MoC, with only a small portion of Pt/Ir atoms showing a CN between 1 and 5 (Fig. 2H, Movie S2). These comprehensive structural analysis results consistently demonstrate that Ir species promoted the dispersion of Pt species on α-MoC to create a high density of interfacial active sites.

Catalytic evaluation

In-situ spectroscopy experiments were performed to examine the potential of the 3Pt3Ir/α-MoC catalyst for activating water and ethanol by tracking the adsorption and evolution of surface species. The O 1s x-ray Photoelectron Spectroscopy (XPS) under ultrahigh vacuum (UHV) showed two peaks at 530.3 and 531.6 eV that we attributed to residual oxygen and hydroxyl groups, respectively, on the surface of α-MoC (Fig. 3A, Fig. S14) (*31*). After dosing water onto the catalyst at room temperature (RT) in near-ambient-pressure XPS (NAP-XPS) experiments, an adsorbed water peak at 533.2 eV(*37*) emerged, accompanied by an increase in the hydroxyl group peak (531.6 eV). This observation suggests that water dissociates into hydroxyl species over 3Pt3Ir/α-MoC at RT, consistent with previous reports on other α-MoC based catalysts (*38*).

In addition, dosing ethanol onto the 3Pt3Ir/α-MoC catalyst at RT caused increases of the two peaks at 531.8 eV and 533.2 eV, attributed to adsorbed oxygenates and ethanol (*39*), respectively (Fig. 3B, Fig. S14), indicating the dissociative adsorption of ethanol. As the temperature increased, the peak assigned to adsorbed oxygenates increased, indicating enhanced activation of ethanol, despite the Pt and Ir species remaining unchanged during this process (Figs. S15 and S16). Meanwhile for $3Pt3Ir/SiO_2$, feeding water and ethanol does not lead to dissociation at RT (Fig. S17). The dissociation of ethanol over the 3Pt3Ir/α-MoC catalysts was further confirmed by transient kinetic analysis (TKA) (Figs. S18 and 19). When C_2H_5OD was fed to the pretreated 3Pt3Ir/α-MoC surface at RT, both H_2 and HD were detected in the outlet gas, suggesting that the catalyst could dissociate both C-H and O-H bonds of ethanol at RT.

To assess the feasibility of ethanol-water partial reforming over these catalysts, we used in-situ Fourier-transforming infrared (FT-IR) spectroscopy (Fig. 3C) to monitor the adsorption (evident by the presence of C-H stretching in ethanol at 2981 cm^{-1}), the effective dehydrogenation of ethanol (evident by the increase of C=O stretching at 1758 cm^{-1}, C-O bending mode at 1377 cm^{-1}, and C-O stretching mode at 1242 cm^{-1} in acetaldehyde (*40*)) and the overall reactivity (formation of acetic acid) among α-MoC, 3Pt3Ir/α-MoC and $3Pt3Ir/SiO_2$ catalysts. For the $3Pt3Ir/SiO_2$ catalyst containing large metal ensembles, the peaks associated with carbon monoxide (C-O

stretching at 2063 cm^{-1}) and methane (C-H stretching at 3016 cm^{-1}, degenerate bending mode at 1303 cm^{-1}) were clearly resolved (Figure 3C(i)) once the vapor of ethanol/water mixture was introduced over the catalyst. This result indicated that large ensembles of noble metals were highly active for C-C bond cleavage (*41*), making them unfavorable for partial ethanol reforming.

In contrast, ethanol dehydrogenation was particularly effective on α-MoC (Figure 3C(ii)), as evidenced by the appearance of bands associated with acetaldehyde at 1242 cm^{-1} and 1758 cm^{-1} after the introduction of the ethanol/water vapor mixture onto the catalyst at 270 °C. Although C-C bond breakage was not observed, we were unable to resolve the peak associated with CH_3COO- over α-MoC, possibly because of its inability to further transform acetaldehyde into the corresponding acid. Surprisingly, only on the 3Pt3Ir/α-MoC catalyst containing abundant atomic-scale interfaces between Pt_1 or Ir_1 and α-MoC , could the asymmetric stretching mode of O=C-O- in CH_3COO- at 1612 cm^{-1} (*42*) be resolved, even from the early stages of reforming (Fig. 3C(iii)). Thus, these interfaces were critical for the formation of acetic acid.

These results demonstrated that the surface of 3Pt3Ir/α-MoC could readily activate both water and ethanol in the initial stage of the reaction, following the pathway shown in Fig. 3C, indicating potentially excellent catalytic performance in steady-state reactions.

The pristine α-MoC sites favored the dehydrogenation of ethanol into acetaldehyde and the dissociation of H_2O into hydroxyls (*31, 43*), whereas the interfaces between atomic-scale Pt or Ir species and α-MoC were pivotal for the partial reforming of ethanol with water. Importantly, eliminating the formation of Pt(Ir)-Pt(Ir) ensembles was crucial for preventing C-C bond cleavage and for the low selectivity toward CO_x and methane in the reaction.

We evaluated the selective reforming performance using a continuous-flow fixed-bed reactor (the mass balance, calculated based on the number of carbon atoms, ranged from 101% to 109% for all catalysts, see Methods for details). Ethanol reforming typically follows a dehydrogenation-reforming sequential pathway (*44*), so the performance of acetaldehyde reforming with water was evaluated first on α-MoC-based catalysts (Fig. 4A). Pure α-MoC shows negligible activity towards acetaldehyde reforming, which is in good agreement with the in-situ FTIR results. In contrast, with the loading of Pt or Ir, the activity increased substantially, suggesting that noble metals or metal/carbide interfaces played a vital role in the reforming process. Although 3Pt/α-MoC showed a higher H_2 production rate than 3Ir/α-MoC, its selectivity toward undesired C_1 products was much higher (~38% vs. ~8%), primarily because of its tendency to aggregate under high metal loadings that promoted C-C bond cleavage. The co-loading of Pt and Ir boosted activity toward H_2 production and high selectivity, exceeding 80%, toward acetic acid. These results supported our proposal that a high density of Pt_1 and Ir_1 single atoms on molybdenum carbide would facilitate H_2 production through reforming while suppressing C-C cleavage.

We then evaluated ethanol reforming with water on these catalysts. Pure α-MoC showed a H_2 production rate of 51.3 $mmol_{H2}/(g_{cat}\cdot h)$ at 543 K, with acetaldehyde as the main product (selectivity ~53.0%) (Figure 4B and Table S4) and ethylene/ethane accounting for ~20% selectivity. Loading

either Pt or Ir onto α-MoC drastically increased the H_2 generation rate (Figs. S20 and S21). A comparison of the reforming activity of Pt/α-MoC and Ir/α-MoC at a low metal loading of 1% (Fig. S22) revealed higher intrinsic ethanol reforming activity for Pt/α-MoC and the essential role of atomic-scale noble-metal/carbide interface in reforming, similar to what we observed for acetaldehyde reforming. For comparison, supporting atomically dispersed Pt species on an inert carbon support yielded neglectable reforming activity, highlighting the essential role of the Pt(or Ir)/α-MoC interface. At a higher metal loading of 3%, both 3Pt/α-MoC and 3Ir/α-MoC demonstrated superior H_2 generation activity (147.3 $mmol_{H2}/(g_{cat}\cdot h)$ and 176.0 $mmol_{H2}/(g_{cat}\cdot h)$, respectively) and a high acetic acid selectivity exceeding 50%. Further increasing the individual metal loading to 6% did not improve the activity or selectivity towards acetic acid (Figs. S20 and S21).

Notably, with co-loading of Pt and Ir, 3Pt3Ir/α-MoC exhibited the highest efficiency, achieving a H_2 generation rate of 331.3 $mmol_{H2}/(g_{cat}\cdot h)$ after optimizing reaction condition (Figs S23 and 24), and surpassed previously reported results in thermocatalysis, photocatalysis and electrocatalysis (Fig. 4D and Tables S5 and S6). A high water-to-ethanol ratio was used (9:1) under the optimal condition, which is critical for both thermodynamic and kinetic reasons, as detailed in the Theoretical Investigation section below. Additionally, 3Pt3Ir/α-MoC demonstrated a high selectivity of 84.5% toward acetic acid, with less than 10% toward C_1 products (CO, CO_2 and CH_4), showing better performance than fully reforming processes under similar reaction temperatures (Figure 4D, Table S7). The presence of a high density of interfacial M_1/α-MoC (M_1 = Pt_1 or Ir_1) sites effectively blocked the undesired reaction routes, such as the formation of acetaldehyde and other by-products.

Durability test on the 3Pt3Ir/α-MoC catalyst demonstrated promising stability in both activity and selectivity over a 100-hour run (Fig. 4C). The activity for H_2 production decreased by 21% from its initial level within the first 100 hours of reaction, but the rate of decline gradually slowed as testing proceeded. Over this period, the catalyst achieved a cumulative H_2 production of 27.3 mol per gram of catalyst, accompanied by the generation of 19.2 mol of acetic acid. Furthermore, XRD characterization revealed no obvious structural change of the catalyst after usage (Fig. S25), suggesting potentially much longer lifespan.

Theoretical investigation

To better understand the enhanced catalytic performance of the 3Pt3Ir/α-MoC catalyst, we performed density functional theory (DFT) calculations to explore the ethanol reforming paths and reaction mechanisms (Fig. 5 and Figs. S26 to S37). With inputs from structural characterizations, we constructed five structural models to represent different catalytic sites: Mo-terminated α-MoC(111) as pristine α-MoC; Pt(111) and Pt(210) representing the flat surface sites and step sites of Pt clusters/particles, respectively; Pt_1/MoC(111) and Ir_1/MoC(111) for atomically dispersed Pt and Ir on α-MoC, respectively.

We first explored the reaction pathways of ethanol decomposition on the α-MoC(111) surface. Figure 5A and Fig. S26 show that on α-MoC(111) the terminal C-H bond of ethanol first dissociated into surface $*CH_2CH_2OH$ and then went through two favored routes. One involved the

dissociation of C-O bond to form ethylene with an effective energy barrier of 0.80 eV, and the other generated the most thermodynamically stable intermediate CH_2CO with an effective energy barrier of 0.78 eV. However, subsequent transformation of this intermediate into acetaldehyde and acetic acid required much higher energy barrier (> 1.3 eV), suggesting that ethanol reforming would be hindered on α-MoC by the accumulation of C_2 species. However, this result did not fully align with the high acetaldehyde selectivity we observed in experiment (Fig. 4B), signaling the strong influence from surface hydroxyls.

Note that under our experimental conditions, a high surface hydroxyl coverage was expected during the reaction because of the high feedstock ratio of water to ethanol (9:1) and the high activity of α-MoC for water dissociation (*31*). To unveil the interaction between carbon intermediates and hydroxyls, we performed calculations of CH_2CH_2OH dissociation on the α-MoC(111) surface with low and high hydroxyl coverages of 1/3 ML and 5/9 ML, respectively (Fig. S27). The rate-determining steps of ethanol decomposition under 5/9 ML hydroxyl coverage are presented in Fig. 5D. A comparison of Fig. 5A with Fig. 5D revealed that the overall energy barrier toward the formation of acetaldehyde was lowered to 0.92 eV at higher hydroxyl coverage, whereas the barrier toward ethylene formation increased to 1.10 eV. This result suggested that ethylene formation could be to some extent inhibited by the increased hydroxyl coverage from water dissociation on α-MoC, consistent with the experimental selectivity.

For comparison, the pathways of ethanol decomposition on Pt particles were also investigated (Fig. 5B and Fig. S28). The results showed that the reforming process on the Pt(111) flat surface did not exhibit a specific preference for any single product, as the calculated energy barriers toward acetaldehyde, acetic acid, CH_2CO intermediate, and C_1 products were similar. However, on the Pt(210) step surface, the energy barrier for C-C bond breakage of the most stable CH_2CO intermediate was reduced to 0.81 eV (Fig. 5C and Fig. S29), suggesting that Pt particles, containing rich step surfaces, favored the formation of C_1 products. This result aligned well with the experimental findings on catalysts containing large metal ensembles, such as the $3Pt3Ir/SiO_2$, 3Pt/α-MoC and 6Pt/α-MoC (Fig. 4B, Fig. S20, and Table S4).

To investigate the catalytic effects of atomic M_1/α-MoC (M_1 = Pt_1 or Ir_1) interfacial sites, we calculated the pathways for the reaction of CH_2CO (the most stable C_2 intermediate on α-MoC, Fig. 5A) into acetic acid and acetaldehyde on Pt_1/MoC(111) and Ir_1/MoC(111) at high hydroxyl coverage (Fig. S30, Fig. 5, E and F). The energy barriers toward the formation of acetic acid were reduced to 0.58 eV on Pt_1/MoC(111) and 0.73 eV on Ir_1/MoC(111), drastically lower than those on pristine α-MoC and metallic Pt surfaces. Thus, the interfacial structure formed by atomically dispersed Pt (or Ir) and α-MoC facilitated the selective generation of acetic acid, aligning well with experimental observations, highlighting the importance of a high density of interfacial M_1/α-MoC sites in turning the reaction pathway towards partial reforming into acetic acid. Our calculations also suggest that small fully exposed metal clusters on MoC exhibit structural and adsorption characteristics (Figs S31 to S37, Movies S3 and S4) akin to those of Pt_1/MoC or Ir_1/MoC sites, thus also contribute to the overall catalytic activity. However, when large Pt or Ir particles form on α-MoC surface, C-C bond cleavage is significantly facilitated, leading to the formation of undesired products like CO_2 and CH_4.

Techno-economic analysis

Having demonstrated the outstanding catalytic performance of 3Pt3Ir/α-MoC in selective partial ethanol reforming, we further conducted an exhaustive techno-economic analysis and life cycle assessment to evaluate its prospect in an industry-scale plant for the production of H_2 and acetic acid (Fig. S31, analysis detailed shown in Tables S8 to S11). The evaluation indicates that the reforming plant can potentially achieve an attractive return on sales (ROS) ratio (Table S12), surpassing the average of the chemical industry (*45*), demonstrating the economic viability of this process. Moreover, over the lifespan of the catalyst, carbon emissions for the production of H_2 and acetic acid are reduced by 21.9% and 38.6%, respectively, compared to conventional routes (Fig. S32, analysis details shown in Table S13). The decrease in fossil energy consumption is even more significant, with reductions of 51% and 86%, respectively. These results provide robust support for the sustainable attributes and feasibility of scaling up this process. Note that this process is still in its primary stage, more research and development efforts are required to further improve its efficiency and adaptability (see Table S12 and associated discussions).

Outlook

In summary, we report a new thermal catalytic process for the selective partial reforming of ethanol with water to produce H_2 and acetic acid, which preserves the carbon resources in a high-valued liquid product and drastically cuts the net carbon emissions. A rational design and construction of a high density of atomic M_1/α-MoC interfacial sites while avoiding the formation of large metal ensembles is demonstrated crucial for tuning the reforming pathway towards a high selectivity of acetic acid and for achieving an unprecedented H_2 generation activity of 331.3 $mmol_{H2}/(g_{cat}\cdot h)$ at low temperatures. This process could be scalable and profitable at an industrial scale, offering a promising avenue for sustainable green H_2 production with zero CO_2 emissions.

References and Notes

1. G. Chen, X. Tu, G. Homm, A. Weidenkaff, Plasma pyrolysis for a sustainable hydrogen economy. *Nature Reviews Materials* **7**, 333-334 (2022).
2. E. Lewis *et al.*, "Comparison of Commercial, State-of-the-Art, Fossil-Based Hydrogen Production Technologies," (2022).
3. I. E. Association, "The Future of Hydrogen," (2019).
4. A. J. Shih *et al.*, Water electrolysis. *Nature Reviews Methods Primers* **2**, (2022).
5. H. de Lasa, E. Salaices, J. Mazumder, R. Lucky, Catalytic steam gasification of biomass: catalysts, thermodynamics and kinetics. *Chem Rev* **111**, 5404-5433 (2011).
6. G. A. Deluga, J. R. Salge, L. D. Schmidt, X. E. Verykios, Renewable hydrogen from ethanol by autothermal reforming. *Science* **303**, 993-997 (2004).
7. L. V. Mattos, G. Jacobs, B. H. Davis, F. B. Noronha, Production of hydrogen from ethanol: review of reaction mechanism and catalyst deactivation. *Chem Rev* **112**, 4094-4123 (2012).
8. A. Palanisamy, N. Soundarrajan, G. Ramasamy, Analysis on production of bioethanol for hydrogen generation. *Environ Sci Pollut Res Int* **28**, 63690-63705 (2021).
9. W. J. Wang, Y. Q. Wang, Thermodynamic analysis of hydrogen production via partial oxidation of ethanol. *Int J Hydrogen Energ* **33**, 5035-5044 (2008).
10. D. Pashchenko, Thermochemical recuperation by ethanol steam reforming: Thermodynamic analysis and heat balance. *Int J Hydrogen Energ* **44**, 30865-30875 (2019).
11. M. Nielsen *et al.*, Low-temperature aqueous-phase methanol dehydrogenation to hydrogen and carbon

dioxide. *Nature* **495**, 85-89 (2013).
12. S. Ogo, Y. Sekine, Recent progress in ethanol steam reforming using non-noble transition metal catalysts: A review. *Fuel Processing Technology* **199**, (2020).
13. E. Balaraman, E. Khaskin, G. Leitus, D. Milstein, Catalytic transformation of alcohols to carboxylic acid salts and H_2 using water as the oxygen atom source. *Nat Chem* **5**, 122-125 (2013).
14. A. C. Dimian, A. A. Kiss, Novel energy efficient process for acetic acid production by methanol carbonylation. *Chemical Engineering Research and Design* **159**, 1-12 (2020).
15. A. L. M. da Silva *et al.*, Cobalt particle size effects on catalytic performance for ethanol steam reforming – Smaller is better. *Journal of Catalysis* **318**, 67-74 (2014).
16. A. L. M. da Silva *et al.*, Oxidative steam reforming of ethanol over carbon nanofiber supported Co catalysts. *Catalysis Today* **164**, 262-267 (2011).
17. A. H. Braga *et al.*, Steam Reforming of Ethanol Using Ni–Co Catalysts Supported on MgAl2O4: Structural Study and Catalytic Properties at Different Temperatures. *ACS Catalysis* **11**, 2047-2061 (2021).
18. M. Martinelli *et al.*, Effect of sodium loading on Pt/ZrO2 during ethanol steam reforming. *Applied Catalysis A: General* **610**, (2021).
19. M. Kourtelesis *et al.*, The effects of support morphology on the performance of Pt/CeO2 catalysts for the low temperature steam reforming of ethanol. *Applied Catalysis B: Environmental* **284**, (2021).
20. H. Meng *et al.*, A strong bimetal-support interaction in ethanol steam reforming. *Nat Commun* **14**, 3189 (2023).
21. W. Shi *et al.*, Modulating Mxene-Derived Ni-Mom-Mo2-mTiC2Tx Structure for Intensified Low-Temperature Ethanol Reforming. *Advanced Energy Materials* **13**, (2023).
22. M. H. Haider *et al.*, Efficient green methanol synthesis from glycerol. *Nat Chem* **7**, 1028-1032 (2015).
23. Y. Deng *et al.*, Molybdenum Carbide: Controlling the Geometric and Electronic Structure of Noble Metals for the Activation of O-H and C-H Bonds. *Acc Chem Res* **52**, 3372-3383 (2019).
24. Y. Ge *et al.*, Maximizing the Synergistic Effect of CoNi Catalyst on alpha-MoC for Robust Hydrogen Production. *J Am Chem Soc* **143**, 628-633 (2021).
25. L. Lin *et al.*, Atomically Dispersed Ni/alpha-MoC Catalyst for Hydrogen Production from Methanol/Water. *J Am Chem Soc* **143**, 309-317 (2021).
26. L. Lin *et al.*, Low-temperature hydrogen production from water and methanol using Pt/alpha-MoC catalysts. *Nature* **544**, 80-83 (2017).
27. M. Compagnoni, A. Tripodi, I. Rossetti, Parametric study and kinetic testing for ethanol steam reforming. *Appl Catal B-Environ* **203**, 899-909 (2017).
28. S. M. de Lima *et al.*, Study of catalyst deactivation and reaction mechanism of steam reforming, partial oxidation, and oxidative steam reforming of ethanol over Co/CeO_2 catalyst. *Journal of Catalysis* **268**, 268-281 (2009).
29. P. S. Kirlin, B. C. Gates, Activation of the C–C bond provides a molecular basis for structure sensitivity in metal catalysis. *Nature* **325**, 38-40 (1987).
30. S. Li *et al.*, Atomically dispersed Ir/alpha-MoC catalyst with high metal loading and thermal stability for water-promoted hydrogenation reaction. *Natl Sci Rev* **9**, nwab026 (2022).
31. X. Zhang *et al.*, A stable low-temperature H(2)-production catalyst by crowding Pt on alpha-MoC. *Nature* **589**, 396-401 (2021).
32. L. Sun *et al.*, High-Efficiency Water Gas Shift Reaction Catalysis on α-MoC Promoted by Single-Atom Ir Species. *ACS Catalysis* **11**, 5942-5950 (2021).
33. M. Peng *et al.*, Fully Exposed Cluster Catalyst (FECC): Toward Rich Surface Sites and Full Atom Utilization Efficiency. *ACS Cent Sci* **7**, 262-273 (2021).
34. Z. Gao, A. Li, D. Ma, W. Zhou, Electron Energy Loss Spectroscopy for Single Atom Catalysis. *Topics in Catalysis* **65**, 1609-1619 (2022).
35. J. Miao, P. Ercius, S. J. L. Billinge, Atomic electron tomography: 3D structures without crystals. *Science* **353**, aaf2157-aaf2157 (2016).
36. Z. Li *et al.*, Probing the atomically diffuse interfaces in Pd@Pt core-shell nanoparticles in three dimensions. *Nat Commun* **14**, 2934 (2023).
37. Z. Liu *et al.*, Water-promoted interfacial pathways in methane oxidation to methanol on a CeO(2)-Cu(2)O catalyst. *Science* **368**, 513-517 (2020).
38. S. Yao *et al.*, Atomic-layered Au clusters on alpha-MoC as catalysts for the low-temperature water-gas shift reaction. *Science* **357**, 389-393 (2017).
39. Z. Liu *et al.*, Ambient pressure XPS and IRRAS investigation of ethanol steam reforming on Ni-CeO2(111) catalysts: an in situ study of C-C and O-H bond scission. *Phys Chem Chem Phys* **18**, 16621-16628 (2016).

40. K. I. Hadjiivanov *et al.*, Power of Infrared and Raman Spectroscopies to Characterize Metal-Organic Frameworks and Investigate Their Interaction with Guest Molecules. *Chem Rev* **121**, 1286-1424 (2021).
41. V. Muravev *et al.*, Size of cerium dioxide support nanocrystals dictates reactivity of highly dispersed palladium catalysts. *Science* **380**, 1174-1179 (2023).
42. X. Q. Tang *et al.*, Co-metal-organic-frameworks with pure uniform crystal morphology prepared via Co(2+) exchange-mediated transformation from Zn-metallogels for luminol catalysed chemiluminescence. *Spectrochim Acta A Mol Biomol Spectrosc* **175**, 11-16 (2017).
43. S. Hanukovich, A. Dang, P. Christopher, Influence of Metal Oxide Support Acid Sites on Cu-Catalyzed Nonoxidative Dehydrogenation of Ethanol to Acetaldehyde. *ACS Catalysis* **9**, 3537-3550 (2019).
44. T. Hou, S. Zhang, Y. Chen, D. Wang, W. Cai, Hydrogen production from ethanol reforming: Catalysts and reaction mechanism. *Renewable and Sustainable Energy Reviews* **44**, 132-148 (2015).
45. N. B. o. S. o. China. (2024), vol. 2024, pp. https://www.stats.gov.cn/english/PressRelease/202402/t20240201_21947130.html.
46. Y. Deng *et al.*, Few-Atom Pt Ensembles Enable Efficient Catalytic Cyclohexane Dehydrogenation for Hydrogen Production. *J Am Chem Soc* **144**, 3535-3542 (2022).
47. M. Newville, IFEFFIT: interactive XAFS analysis and FEFF fitting. *J Synchrotron Radiat* **8**, 322-324 (2001).
48. J. J. Rehr, R. C. Albers, S. I. Zabinsky, High-order multiple-scattering calculations of x-ray-absorption fine structure. *Phys Rev Lett* **69**, 3397-3400 (1992).
49. M. Bosman, M. Watanabe, D. T. Alexander, V. J. Keast, Mapping chemical and bonding information using multivariate analysis of electron energy-loss spectrum images. *Ultramicroscopy* **106**, 1024-1032 (2006).
50. K. Dabov, A. Foi, V. Katkovnik, K. Egiazarian, Image Denoising by Sparse 3-D Transform-Domain Collaborative Filtering. *IEEE Transactions on Image Processing* **16**, 2080-2095 (2007).
51. Y. Yang *et al.*, Determining the three-dimensional atomic structure of an amorphous solid. *Nature* **592**, 60-64 (2021).
52. S. S. Rogers, T. A. Waigh, X. Zhao, J. R. Lu, Precise particle tracking against a complicated background: polynomial fitting with Gaussian weight. *Physical Biology* **4**, 220-227 (2007).
53. A. T. Brünger *et al.*, Crystallography & NMR System: A New Software Suite for Macromolecular Structure Determination. *Acta Crystallographica Section D Biological Crystallography* **54**, 905-921 (1998).
54. S. Lloyd, Least squares quantization in PCM. *IEEE Transactions on Information Theory* **28**, 129-137 (1982).
55. J. Zhou *et al.*, Observing crystal nucleation in four dimensions using atomic electron tomography. *Nature* **570**, 500-503 (2019).
56. C. Q. Song *et al.*, Photothermal Conversion of CO with Tunable Selectivity Using Fe-Based Catalysts: From Oxide to Carbide. *Acs Catalysis* **10**, 10364-10374 (2020).
57. G. Kresse, J. Furthmuller, Efficiency of ab-initio total energy calculations for metals and semiconductors using a plane-wave basis set. *Comp Mater Sci* **6**, 15-50 (1996).
58. G. Kresse, J. Furthmuller, Efficient iterative schemes for ab initio total-energy calculations using a plane-wave basis set. *Phys Rev B Condens Matter* **54**, 11169-11186 (1996).
59. P. E. Blochl, Projector augmented-wave method. *Phys Rev B Condens Matter* **50**, 17953-17979 (1994).
60. G. Kresse, D. Joubert, From ultrasoft pseudopotentials to the projector augmented-wave method. *Phys Rev B* **59**, 1758-1775 (1999).
61. J. P. Perdew, K. Burke, M. Ernzerhof, Generalized Gradient Approximation Made Simple. *Physical Review Letters* **77**, 3865-3868 (1996).
62. G. Henkelman, B. P. Uberuaga, H. Jónsson, A climbing image nudged elastic band method for finding saddle points and minimum energy paths. *The Journal of Chemical Physics* **113**, 9901-9904 (2000).
63. M. Younas, S. Shafique, A. Hafeez, F. Javed, F. Rehman, An Overview of Hydrogen Production: Current Status, Potential, and Challenges. *Fuel* **316**, (2022).
64. P. Khamhaeng, N. Laosiripojana, S. Assabumrungrat, P. Kim-Lohsoontorn, Techno-economic analysis of hydrogen production from dehydrogenation and steam reforming of ethanol for carbon dioxide conversion to methanol. *Int J Hydrogen Energ* **46**, 30891-30902 (2021).
65. P. Zhou *et al.*, Partially reduced Pd single atoms on CdS nanorods enable photocatalytic reforming of ethanol into high value-added multicarbon compound. *Chem* **7**, 1033-1049 (2021).
66. Y. Chao *et al.*, Visible-Light Direct Conversion of Ethanol to 1,1-Diethoxyethane and Hydrogen over a Non-Precious Metal Photocatalyst. *Chemistry – A European Journal* **25**, 189-194 (2018).
67. M. J. Sampaio *et al.*, Photocatalytic performance of Au/ZnO nanocatalysts for hydrogen production from ethanol. *Applied Catalysis A: General* **518**, 198-205 (2016).
68. C. Xing *et al.*, A Direct Z-Scheme for the Photocatalytic Hydrogen Production from a Water Ethanol Mixture on CoTiO3/TiO2 Heterostructures. *ACS Applied Materials & Interfaces* **13**, 449-457 (2021).

69. X. Zhang *et al.*, Increasing the Activity and Selectivity of TiO2-Supported Au Catalysts for Renewable Hydrogen Generation from Ethanol Photoreforming by Engineering Ti3+ Defects. *ACS Sustainable Chemistry & Engineering* **7**, 13856-13864 (2019).
70. A. V. Puga, A. Forneli, H. García, A. Corma, Production of H2 by Ethanol Photoreforming on Au/TiO2. *Advanced Functional Materials* **24**, 241-248 (2013).
71. A. H. Jawhari, N. Hasan, I. A. Radini, M. A. Malik, K. Narasimharao, Pt-Ag/Ag3PO4-WO3 nanocomposites for photocatalytic H2 production from bioethanol. *Fuel* **344**, (2023).
72. S. Luo *et al.*, Solar-driven production of hydrogen and acetaldehyde from ethanol on Ni-Cu bimetallic catalysts with solar-to-fuels conversion efficiency up to 3.8 %. *Applied Catalysis B: Environmental* **272**, (2020).
73. E. Bu *et al.*, Effect of the TiO2-carbon interface on charge transfer and ethanol photo-reforming. *Catalysis Today* **422**, (2023).
74. S. Sheng *et al.*, Rational design of Co-S-P nanosheet arrays as bifunctional electrocatalysts for both ethanol oxidation reaction and hydrogen evolution reaction. *Inorganic Chemistry Frontiers* **7**, 4498-4506 (2020).
75. X. Zhao *et al.*, Self-Supported 3D PdCu Alloy Nanosheets as a Bifunctional Catalyst for Electrochemical Reforming of Ethanol. *Small* **13**, (2017).
76. Y. X. Chen *et al.*, Nanotechnology makes biomass electrolysis more energy efficient than water electrolysis. *Nature Communications* **5**, (2014).
77. H. A. Miller, M. Bellini, F. Vizza, C. Hasenöhrl, R. D. Tilley, Carbon supported Au–Pd core–shell nanoparticles for hydrogen production by alcohol electroreforming. *Catalysis Science & Technology* **6**, 6870-6878 (2016).
78. M.-X. Gu *et al.*, Highly Dispersive Cobalt Oxide Constructed in Confined Space for Oxygen Evolution Reaction. *ACS Sustainable Chemistry & Engineering* **7**, 2837-2843 (2019).
79. L. Dai *et al.*, Electrochemical Partial Reforming of Ethanol into Ethyl Acetate Using Ultrathin Co3O4 Nanosheets as a Highly Selective Anode Catalyst. *ACS Central Science* **2**, 538-544 (2016).
80. J. Y. Z. Chiou *et al.*, Pathways of ethanol steam reforming over ceria-supported catalysts. *Int J Hydrogen Energ* **37**, 13667-13673 (2012).
81. V. Palma, F. Castaldo, P. Ciambelli, G. Iaquaniello, CeO-supported Pt/Ni catalyst for the renewable and clean H production via ethanol steam reforming. *Appl Catal B-Environ* **145**, 73-84 (2014).
82. V. V. Galvita *et al.*, Ethanol decomposition over Pd-based catalyst in the presence of steam. *Reaction Kinetics and Catalysis Letters* **76**, 343-351 (2002).
83. B. S. Kwak, J. Kim, M. Kang, Hydrogen production from ethanol steam reforming over core–shell structured NixOy–, FexOy–, and CoxOy–Pd catalysts. *Int J Hydrogen Energ* **35**, 11829-11843 (2010).
84. C. G. Alonso, A. C. Furtado, M. P. Cantao, O. A. A. dos Santos, N. R. C. Fernandes-Machado, Temperature Effect on Hydrogen Production from Reactions between Ethanol and Steam in the Presence of Pd-Ru/NbO-TiO Catalyst. *Int J Chem React Eng* **7**, (2009).
85. A. Ciftci, D. A. J. M. Ligthart, P. Pastorino, E. J. M. Hensen, Nanostructured ceria supported Pt and Au catalysts for the reactions of ethanol and formic acid. *Appl Catal B-Environ* **130**, 325-335 (2013).
86. K. H. Lin, C. B. Wang, S. H. Chien, Catalytic performance of steam reforming of ethanol at low temperature over LaNiO perovskite. *Int J Hydrogen Energ* **38**, 3226-3232 (2013).
87. J. Sun, D. F. Luo, P. Xiao, J. G. Li, S. Yu, High yield hydrogen production from low CO selectivity ethanol steam reforming over modified Ni/YO catalysts at low temperature for fuel cell application. *J Power Sources* **184**, 385-391 (2008).
88. H. Inokawa, S. Nishimoto, Y. Kameshima, M. Miyake, Promotion of H production from ethanol steam reforming by zeolite basicity. *Int J Hydrogen Energ* **36**, 15195-15202 (2011).
89. N. Homs, J. Llorca, P. R. de la Piscina, Low-temperature steam-reforming of ethanol over ZnO-supported Ni and Cu catalysts - The effect of nickel and copper addition to ZnO-supported cobalt-based catalysts. *Catalysis Today* **116**, 361-366 (2006).

Acknowledgments: NAP-XPS experiments were conducted at BL02B of Shanghai Synchrotron Radiation Facility and the Analytical Instrumentation Center of Peking University. The authors thank Yao Xu for helping with the NAP-XPS experiments. XAFS experiments were conducted at BL39XU of SPring-8 with the approval of the Japan Synchrotron Radiation Research Institute (JASRI) (Proposal No. 2019B1237) and Beijing Synchrotron Radiation Facility. This research benefited from resources and supports from the Electron Microscopy Center at the University of

Chinese Academy of Sciences. The authors thank the Electron Microscopy Laboratory and the Analytical Instrumentation Center at Peking University for the use of aberration-corrected electron microscopes for AET experiment, and the High-performance Computing Platform of Peking University for 3D reconstruction. D. M. acknowledges support from the Tencent Foundation through the XPLORER PRIZE and New Cornerstone Investigator Program. The authors thank Mark Howard, Jie Su, and Yi Qiu for the helpful discussion.

Funding:

National Key R&D Program of China 2023YFA1506602 (MP), 2021YFA1501102 (DM)

CAS Project for Young Scientists in Basic Research (YSBR-003) (WZ)

National Natural Science Foundation of China 22232001 (DM), 22202004 (MP), 22172003 (JZ), 22172083(RG)

XPLORER Prize of Tencent Foundation (DM)

New Cornerstone Science Foundation of Tencent Foundation (DM)

Liaoning Binhai Laboratory LBLF-2023-02 (DM)

Author contributions:

Conceptualization: DM, GJH, WZ

Methodology: WZ, JZ, AH, JD, JY, RG, HZ, LZ

Investigation: MP, YG, AL, ZX, QY

Visualization: MP, AL, ZX, JZ, QZ

Funding acquisition: DM, WZ, MP, JZ

Project administration: DM

Supervision: DM, WZ

Writing – original draft: MP, JZ, AL

Writing – review & editing: MP, JZ, AL, WZ, DM

Competing interests: A Chinese patent that covers the PtIr/α-MoC catalysts reported in this paper was filed by Peking University (application no. 202411426363.1). Other than this, the authors declare that they have no competing interests.

Data and materials availability: All data supporting the findings of this study are available within the paper and its supplementary materials.

Supplementary Materials

Materials and Methods

Figs. S1 to S39

Tables S1 to S13

References (*46*–*89*)

Movies S1 to S4

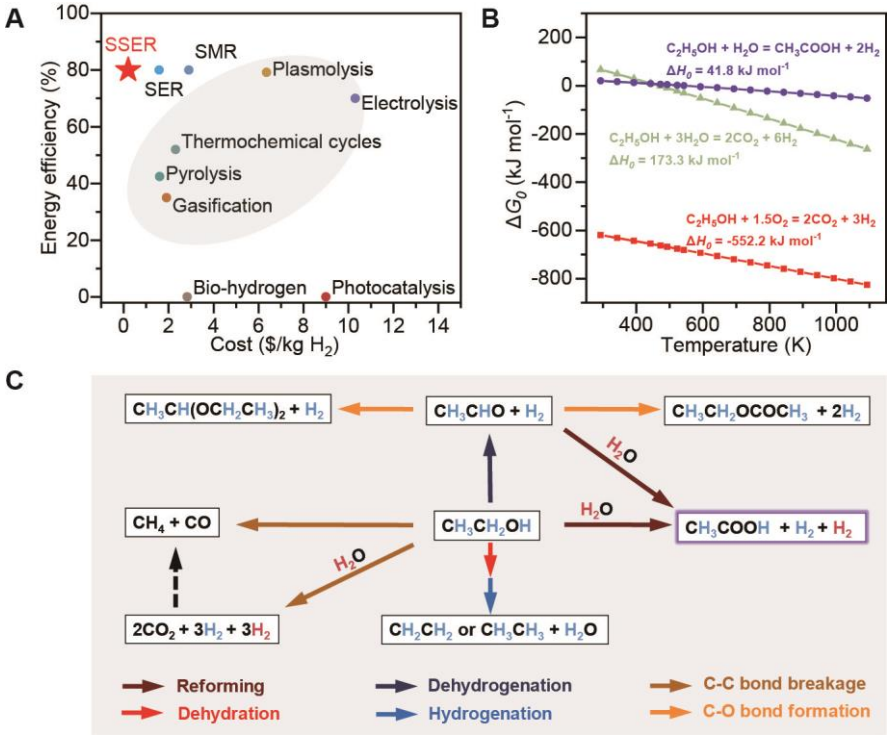

Fig. 1. A survey of H_2 production routes. (**A**) Comparison of energy efficiency and costs of various H_2 production routes. Detailed references listed in Table S1. SMR: steam methanol reforming; SER: steam ethanol reforming; SSER: selective steam ethanol reforming. (**B**) Thermodynamics evaluation of different ethanol conversion routes. (**C**) Schematics of the reaction network for ethanol reforming: (i) ethanol convert into acetaldehyde via dehydrogenation and forms the corresponding (hemi)acetal through condensation, with the latter not contributing to net H_2 production; (ii) ethanol goes through dehydration/hydrogenation to form ethylene and ethane, neither generating H_2; (iii) ethanol can produce CO_2 and CO/CH_4 via C-C bond breakage, a side reaction consuming H_2; (iv) ethanol goes through full reforming with water and produces H_2 and CO_2. Although this process produces the most H_2, it requires higher temperatures and does not preserve the carbon resource at all; and (v) ethanol selectively reforms with water to produce H_2 from both reactants while preserving high-value C_2 products such as acetic acid.

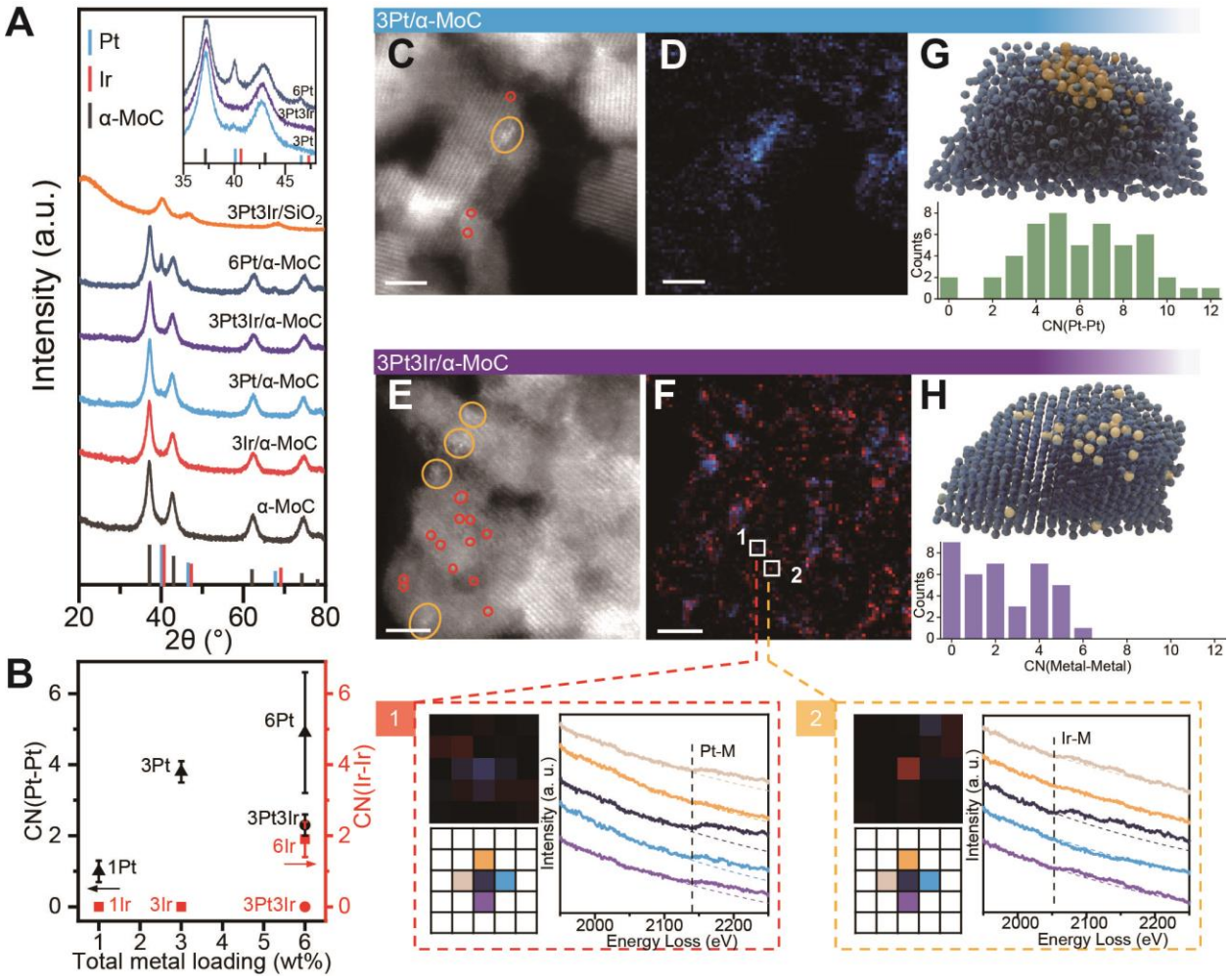

Fig. 2. Structural characterization of the PtIr/α-MoC catalysts. (**A**) XRD profiles of α-MoC supported Pt/Ir catalysts with different metal loadings. Inset notes the enlarged region of the Pt(111) diffraction peak. (**B**) Coordination numbers (CN) of Pt-Pt and Ir-Ir in different catalysts obtained from EXAFS fitting. ▲: Pt/α-MoC, ■: Ir/α-MoC, ●: PtIr/α-MoC. (**C, D**) HAADF image (C) and the corresponding EELS mapping (D) of 3Pt/α-MoC. (**E, F**) HAADF image (E), and the corresponding EELS mapping (F) of 3Pt3Ir/α-MoC. Metal clusters and atomically dispersed species are marked with yellow and red circles, respectively. Pt element is presented in blue and Ir in red in the EELS mapping. The bottom panels present the enlarged Pt/Ir elemental maps and the corresponding pixel indexes of the areas marked by the white squares 1 and 2 in panel F, and the EELS spectra extracted from the pixels with the corresponding colors. (**G, H**) The metal atom distribution in 3Pt/α-MoC (G) and 3Pt3Ir/α-MoC (H) obtained through 3D reconstruction from tomographic tilt series. The blue spheres show Mo atoms, and the golden spheres represent Pt/Ir atoms. The bar charts show the M-M (M=Pt or Ir) coordination number distribution calculated from the reconstructed 3D structural model. Scale bars in panels C-F: 2 nm.

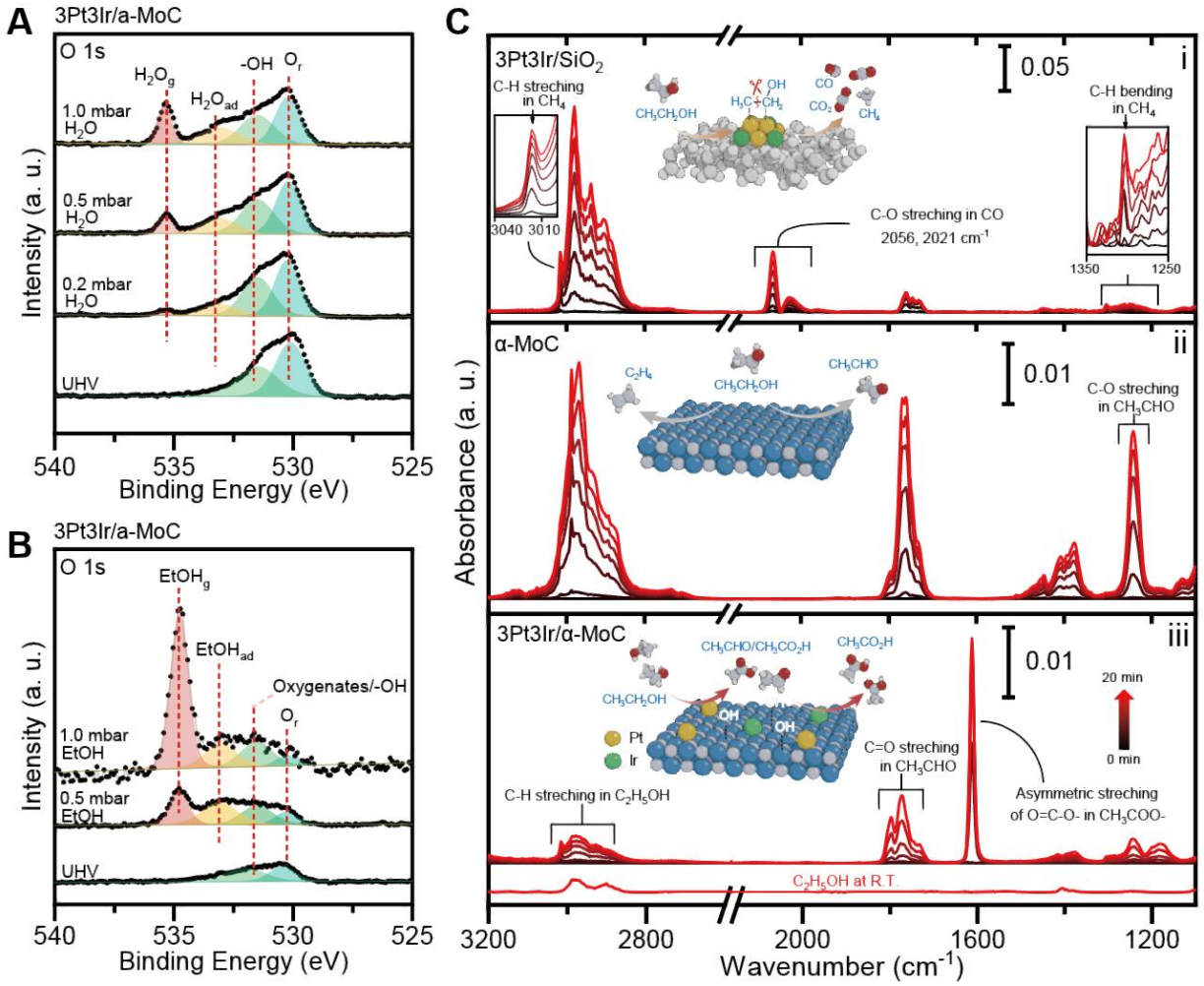

Fig. 3. Reaction network and site requirement studies for partial reforming of ethanol. (**A-B**) NAP-XPS results of the 3Pt3Ir/α-MoC catalyst under different pressure of H_2O (A) and ethanol (B). The samples were treated in the corresponding environments noted in the figure for 30 min before measuring. O_r represents residual oxygen; H_2O_g and H_2O_{ad} denote water in the gas phase and water adsorbed on the catalyst surface, respectively; $EtOH_g$ and $EtOH_{ad}$ refer to ethanol in the gas phase and ethanol adsorbed on the catalyst surface, respectively. (**C**) In-situ FTIR spectra of water and ethanol adsorption over (i) 3Pt3Ir/SiO_2, (ii) α-MoC**,** and (iii) 3Pt3Ir/α-MoC catalysts at 270 °C. The fresh catalysts after pretreatment were followed by Ar flushing for 30 min at 270 °C, and then exposed to ethanol and water atmosphere. Inset includes schematic illustration of possible dominant reaction pathways on each catalyst.

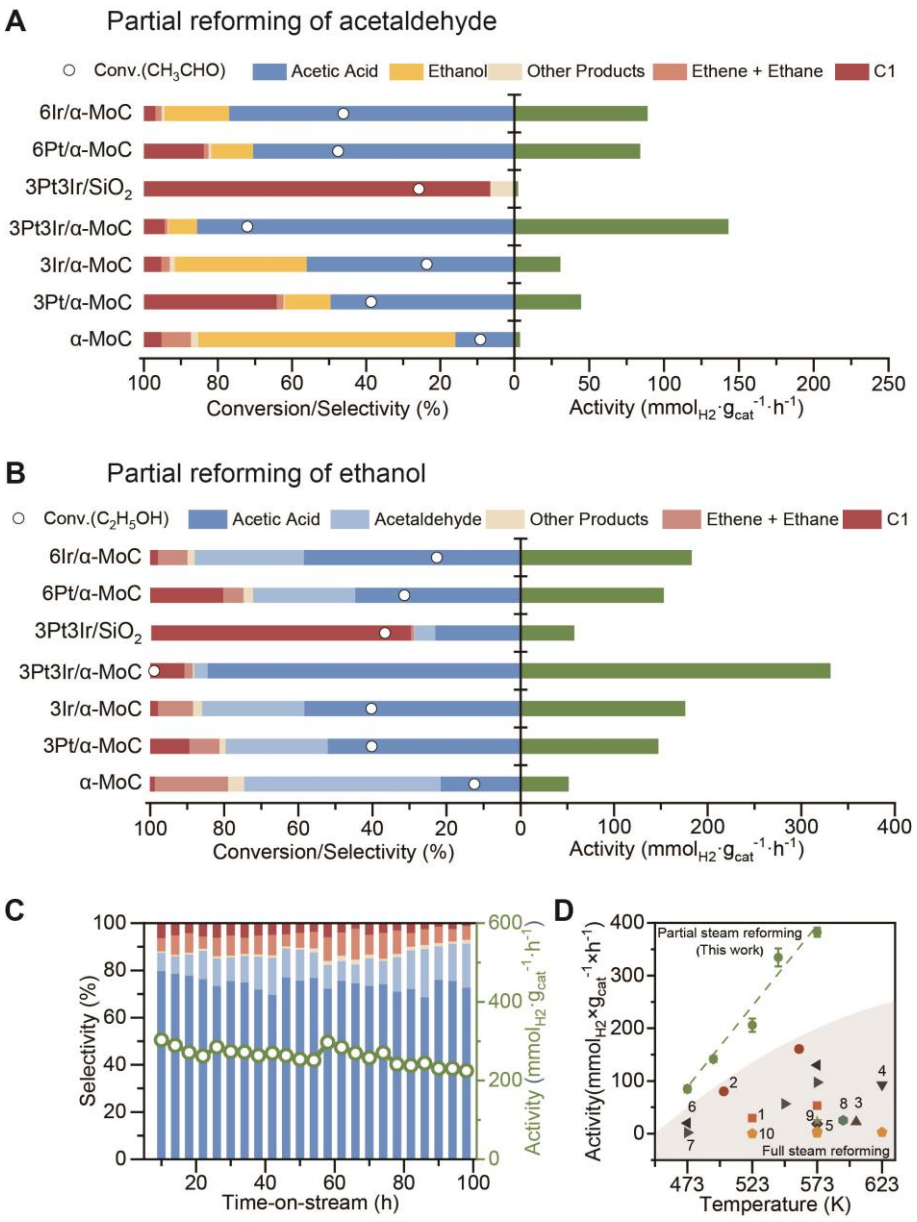

Fig. 4. Catalytic performance for partial reforming of ethanol. (**A**) Catalytic performance of supported Pt/Ir catalysts for partial reforming of acetaldehyde. Reaction conditions: 543 K, weight-hourly space velocity (WHSV) of acetaldehyde = 10.6 $g_{acetaldehyde}/(g_{cat} \cdot h)$, flow rate of the carrier gas (5% Ar in N_2) = 60 mL/min, n (acetaldehyde) : n (H_2O) = 1 : 9 . (**B**) Catalytic performance of supported Pt/Ir catalysts for partial reforming of ethanol. Reaction conditions: 543 K, $WHSV_{ethanol}$ = 10.6 $g_{ethanol}/(g_{cat} \cdot h)$, flow rate of the carrier gas (5% Ar in N_2) = 60 mL/min, n (ethanol) : n (H_2O) = 1 : 9 . (**C**) Long-term stability test of 3Pt3Ir/α-MoC for partial reforming of ethanol with water. The reaction condition is the same as in panel B. (**D**) Comparison of H_2 production activity through ethanol steam reforming in literature and in this work. The same symbol indicates data from the same reference (detailed references are listed in Table S7) .

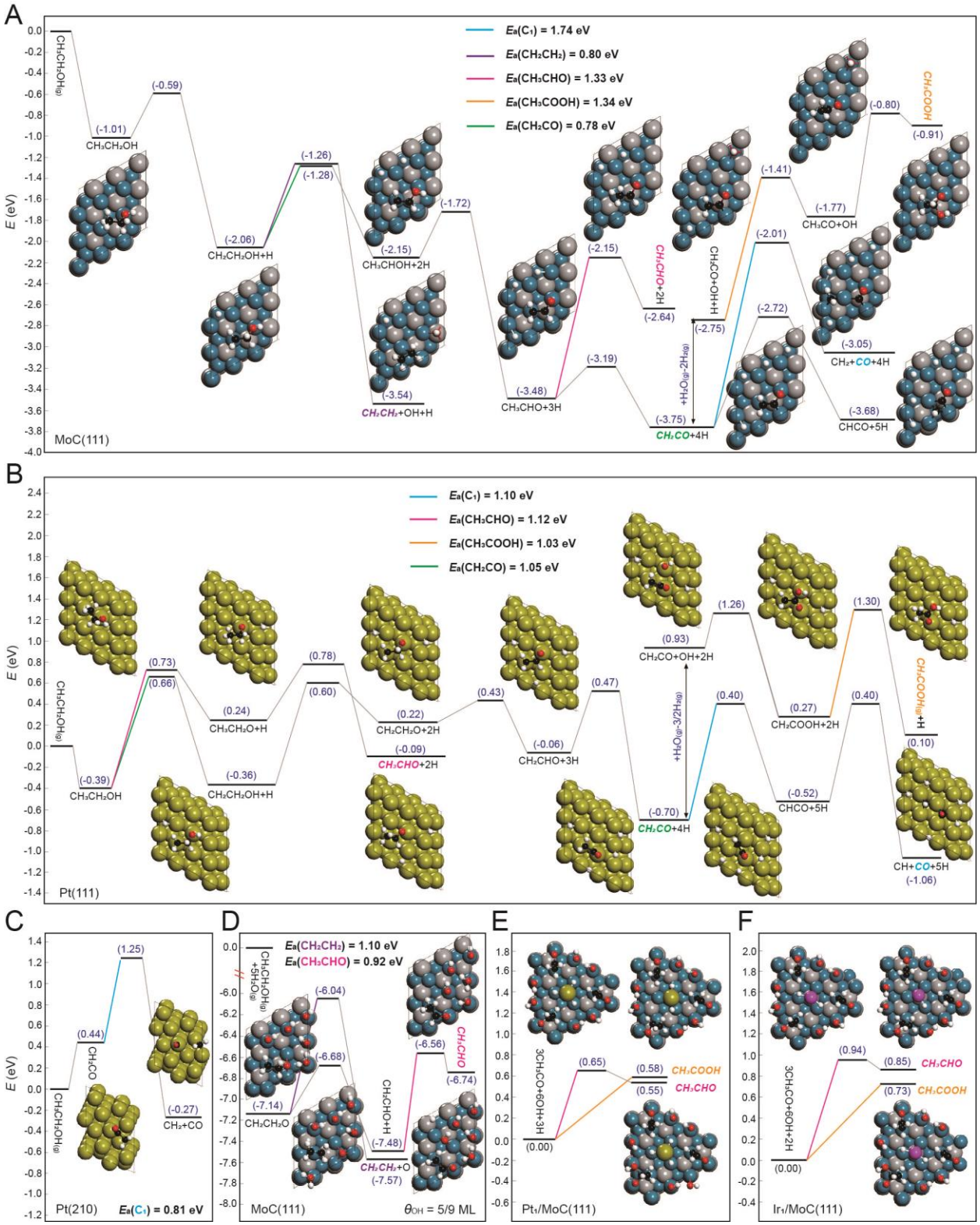

Fig. 5. Reaction pathways of ethanol reforming on PtIr/α-MoC catalysts. (**A**) Energy profiles for ethanol conversion pathways on the pure α-MoC (111) surface; (**B**) Energy profiles for ethanol conversion pathways on the flat Pt(111) surface; (**C**) Energy profile for the conversion pathway of the most stable intermediate CH_2CO on the Pt(210) step surface; (**D**) Energy profiles for the

corresponding formation pathways of C_2H_4 and CH_3CHO on the α-MoC(111) surface with a hydroxyl coverage of 5/9 ML; (**E, F**) the energy profiles for the rate-determining steps of CH_3CHO and CH_3COOH formation from the most stable intermediate CH_2CO and hydroxyl on the Pt_1/MoC(111) (E) and Ir_1/MoC(111) (F) interfaces (CH_2CO/OH = 1:2, their total coverage = 9/16 ML). The Pt, Ir, Mo, C, O and H atoms are shown in gold, pink, dark cyan, grey, red, and white, respectively; to make a distinguish, the C atoms from ethanol are marked in black.